Aeroelastic Analysis of Aircraft Wings

André de Sousa Cardeira
andre.cardeira@tecnico.ulisboa.pt

Instituto Superior Técnico, Lisboa, Portugal

December 2014

Abstract

Aeroelasticity phenomena involve the study of the interaction between aerodynamic and elastic forces (static aeroelasticity), and aerodynamic, inertial, and elastic forces (dynamic aeroelasticity). Modern aircraft structures, making more and more use of lightweight composite structures, may be very flexible making the aeroelastic study an important aspect of the aircraft design.

Flutter is a dynamic aeroelastic instability characterized by sustained oscillation of structure arising from interaction between those three forces acting on the body. The present work aims to study the flutter behavior on three-dimensional subsonic aircraft wings, using a computationally efficient method. For that, a new computational aeroelasticity design framework was created using a panel method to solve the fluid flow approximated as potential flow and a commercial software for the structural analysis. A validation of the fluid solver is made using wind tunnel data, while the structure solver is verified using the available tests. The coupling of the two domains is made with a main script using an adequate time discretization scheme.

The results are presented for a wing example which is denoted as reference case. Later, a study of the influence of pertinent parameters is performed, concluding with the comparison between the many values tested. It is concluded that the framework shows very good agreement to the theoretical influences of the parameters studied. Despite the simplification of the fluid flow, which was assumed to be potential, this method proves to be a very useful tool in aircraft preliminary design.
Keywords: Aeroelasticity, Panel method, Fluid-structure interaction, Finite element method, Flutter, Divergence velocity.

1. Introduction

Structural analyses constitute a crucial part in Aircraft Design. Since the primordials of the aviation history, it was stated that the success of the air vehicle is dependent on a structure capable of withstanding the several loads encountered in each flight and a strong propulsion system. Moreover, both components should be as light as possible.

Aeroelastic phenomena in modern high-speed aircraft have profound upon the design of structural members and also upon mass distribution, lifting surface planforms and control system design [3]. Accurate computational aeroelastic tests can be applied in early stages of the design phase. By increasing the accuracy and feasibility of computational tools, one can decrease the number of experimental tests needed, which largely reduces the design costs. Also, applications of the aeroelastic phenomena are found in several other disciplines.

A general (but complete) definition is the one from [6]:

The science of aeroelasticity encompasses those physical processes and problems that result from the interaction between elasto-mechanical systems and the surrounding airflow.

To help visualizing the context of the term, a representation in triangle is used, presented in Figure 1.

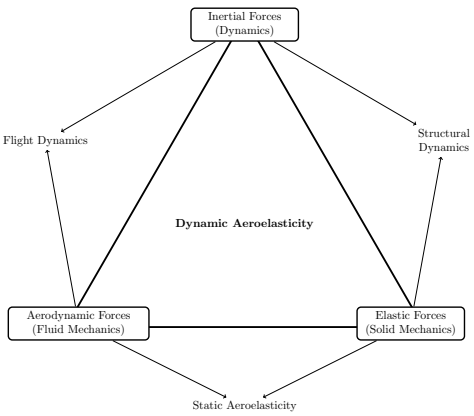

Figure 1: Collar triangle.

By pairing two of the three corners of the triangle,

one can identify other important disciplines. For example,

- Aerodynamics + dynamics = aerodynamic stability;
- Dynamics + solid mechanics = structural dynamics;
- Aerodynamics + solid mechanics = static aeroelasticity.

In some sense, all these technical fields may be considered special cases of aeroelasticity. However, for dynamic aeroelastic effects to occur, all three forces are required.

Flutter has perhaps the most far-reaching effects on high-speed aircraft [3]. The *classical* type of flutter is associated with potential flow and usually, involves coupling of two or more degrees of freedom (DOF). The *nonclassical* type of flutter may involve separated flow, turbulence and stalling conditions.

The object of study is the aircraft wing. The main structural parts are the spars, ribs, stringers and the skin. Then, accordingly to the application, one can change their materials, quantity, location and so on.

A simplified structure is used with only two spars and a skin. The skin will then be thicker to compensate the absence of stringers and the spars can be moved forward and backward to manipulate the torsional characteristics of the wing.

The objectives of this work are then to review the actual models and methods to compute aeroelastic calculations, state the governing equations and its acceptable approximations, and to apply some of these methods to perform aeroelastic studies of aircraft wings.

For these studies, an available tool for structural analysis are employed (CSM), while the aerodynamic (CFD) and coupling tools are to be created and merged in a computational program. The final result is an aeroelastic design framework for subsonic aircraft wings.

2. Background

For the aeroelastic design framework, three domains of theory are treated: structural, fluid flow and fluid-structure coupling.

2.1. Structural Approach

The transient dynamic equilibrium equation is, for a linear structure, as follows

$$M\ddot{\vec{u}} + C\dot{\vec{u}} + K\vec{u} = \vec{F}, \tag{1}$$

where M represents the structural mass matrix, C the structural damping matrix, K the structural stiffness matrix, $\ddot{\vec{u}}$ the nodal acceleration vector, $\dot{\vec{u}}$ the nodal velocity vector, $\vec{u}$ the nodal displacement vector and $\vec{F}$ the applied load vector.

In this work, the structural computations are made in the commercial software ANSYS Parametric Design Language (APDL). It has available two time integration schemes [1], being the most commonly used the implicit Newmark method, which applied to the Equation (1) gives

$$\begin{aligned} \vec{u}_{n+1}\left(a_0 M + a_1 C + K\right) = \vec{F} + \\ M\left(a_0\vec{u}_n + a_2\dot{\vec{u}}_n + a_3\ddot{\vec{u}}_n\right) + , \\ C\left(a_1\vec{u}_n + a_4\dot{\vec{u}}_n + a_5\ddot{\vec{u}}_n\right) \end{aligned} \tag{2}$$

where

$$\begin{aligned} a_0 &= \frac{1}{\alpha\Delta t^2}, & a_1 &= \frac{\delta}{\alpha\Delta t}, \\ a_2 &= \frac{1}{\alpha\Delta t}, & a_3 &= \frac{1}{2\alpha} - 1, \\ a_4 &= \frac{\delta}{\alpha} - 1, & a_5 &= \frac{\Delta t}{2}\left(\frac{\delta}{\alpha} - 2\right), \\ a_6 &= \Delta t\left(1 - \delta\right), & a_7 &= \delta\Delta t. \end{aligned}$$

As documented in [1], this scheme is unconditionally stable for

$$\alpha \geq \frac{1}{4}\left(\frac{1}{2} + \delta\right)^2, \quad \delta \geq \frac{1}{2}, \quad \frac{1}{2} + \delta + \alpha > 0, \tag{3}$$

where α and δ are the Newmark integration parameters and are related to the amplitude decay factor γ by $\alpha = \frac{1}{4}(1+\gamma)^2$ and $\delta = \frac{1}{2} + \gamma$.

Three methods are available in APDL to solve the equation (2): the full, reduced and mode superposition. The full method simply solves (2) with no additional assumptions, while the reduced forbids the use of pressure loads and the mode superposition has no element damping matrices. So, the full method is the one used for this task.

All the model will be constructed with SHELL181 elements. It is a four-node quadrilateral bi-linear element with six DOF at each node: translations in the x, y, and z directions and rotations about the x, y and z-axes.

2.2. Aerodynamic Approach

For the aerodynamic calculations, the *Potential Flow Model* is here applied. It is obtained assuming that the flow is inviscid, irrotational and isentropic. Compressible effects are out of the scope of this thesis, so the fluid is also assumed incompressible. With these assumptions, the governing equation is

$$\nabla \cdot \vec{V} = \nabla \cdot (\nabla \cdot \Phi) = \nabla^2\Phi = 0, \tag{4}$$

where $\Phi(x, y, z)$ is the velocity potential. Equation (4) is a linear differential equation known as *Laplace*

equation. It was extensively studied and it has many possible analytical solutions. Also, because it is linear, the *principle of superposition* applies. This means that if Φ_1, Φ_2, ..., Φ_n are solutions of the Laplace equation, then

$$\Phi = \sum_{k=1}^{n} c_k \Phi_k \tag{5}$$

is also a solution for it (c_k are arbitrary constants).

The boundary conditions for this problem are the impermeability condition (zero normal velocity on a body) and the far field condition (the disturbance created by the motion should vanish far from the body).

The solutions in evidence here are the Source

$$\Phi = -\frac{\sigma}{4\pi \left|\vec{r} - \vec{r_0}\right|} \tag{6}$$

and the Doublet

$$\Phi = \frac{\mu}{4\pi} \frac{\partial}{\partial n} \frac{1}{|\vec{r} - \vec{r_0}|}, \tag{7}$$

where σ and ν are the source and doublet strength, respectively.

The pressure computation is made using the *Bernoulli equation* for inviscid incompressible irrotational flow,

$$E + \frac{p}{\rho} + \frac{V^2}{2} + \frac{\partial \Phi}{\partial t} = C(t). \tag{8}$$

This means that at a certain time t_1, the quantity at the left-hand side of Equation (8) must be equal throughout the field. Particularly, one can compare any point of the field with a reference point. If this reference condition is chosen such that $E = 0$ (no body forces) and $\Phi_\infty = const.$, then the pressure coefficient C_p at any point can be calculated from

$$C_p = \frac{p - p_\infty}{0.5\rho V_\infty^2} = 1 - \frac{V^2}{V_\infty^2} - \frac{2}{V_\infty^2} \frac{\partial \Phi}{\partial t}. \tag{9}$$

The integration over time demands a time discretization method. Since the goal is to obtain the pressure coefficient at the time $t + \Delta t$, an implicit method is required. The simpler and still largely used option is the *Backward Euler Method* [5], which applied to Equation (9) yields

$$C_p^{t+\Delta t} = 1 - \frac{(V^{t+\Delta t})^2}{V_\infty^2} - \frac{2}{V_\infty^2} \left(\frac{\Phi^{t+\Delta t} - \Phi^t}{\Delta t} \right), \tag{10}$$

which is first order accurate. A second order accurate possibility is the *Crank-Nicholson Method*[5].

From here, a panel method was built based on the formulation from Katz and Plotkin [7] using constant quadrilateral sources and doublets. The Dirichlet boundary condition results in the form

$$\begin{array}{l} \frac{1}{4\pi} \int_{body+wake} \mu \vec{n} \cdot \nabla \left(\frac{1}{r} \right) dS - \\ \frac{1}{4\pi} \int_{body} \sigma \left(\frac{1}{r} \right) dS = 0 \end{array} . \tag{11}$$

The body surface is now discretized into N surface panels and the wake is modeled using N_W panels. This problem is then reduced to a set of linear algebraic equations

$$\sum_{k=1}^{N} C_k \mu_k + \sum_{l=1}^{N_W} C_l \mu_l + \sum_{k=1}^{N} B_k \sigma_k = 0, \tag{12}$$

where for each collocation point the summation of the influences of all k body panels and l wake panels is needed. Since the singularity elements have constant strength in each panel, the integrals depend only on the geometry.

For Equation (11) to be valid and from the definition of the source strength σ, it comes an additional condition that

$$\sigma = \vec{n} \cdot \vec{V}_\infty. \tag{13}$$

And this way the third term on Equation (12) is calculated and can be moved to the right-hand side.

The influence from the wake comes from the linear Kutta condition

$$\mu_W = \mu_U - \mu_L, \tag{14}$$

where μ_U and μ_L are the upper and lower surface doublet strengths at the trailing edge and μ_W is constant along the wake (in a steady problem).

In an unsteady case, the wake shape is obtained using a *time-stepping method*. Herein the wake is directly related to the motion, being convected with $\vec{V}_\infty$ at each time step.

2.3. Fluid-Structure Coupling

The coupling between fluid and strutural domains is normally referred as *Fluid-Structure Interaction* (FSI). The range of FSI models can be divided in two categories: strongly-coupled (or monolithic) and loosely-coupled (or staggered). A monolithic approach would be for this case, to merge Equations (1) and (9) and to integrate over time.

The other option is a staggered procedure. For a given time step, such an algorithm typically involves the solution of the fluid mechanics with the velocity boundary conditions coming from the previous step, followed by the solution of the structural mechanics equations with the updated fluid interface load, and followed by the mesh movement with the new structure displacement.

The basic algorithm is the so called *Conventional Serial Staggered (CSS)* procedure [4]. It is graphically depicted in Figure 2, where $\vec{\mathcal{U}}$ denotes the

structure state vector (nodal displacement and velocity), $\vec{\mathcal{W}}$ denotes the fluid state vector (in the case of a complete fluid discretization), $\vec{p}$ designates the fluid pressure, n stands for the n^{th} time station, and the equalities shown at the top hold on the fluid/structure interface boundary.

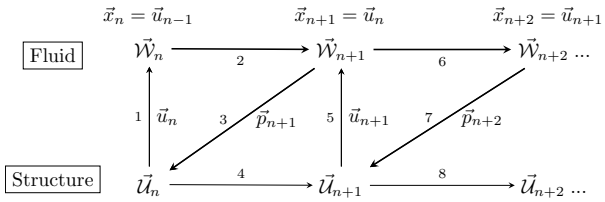

Figure 2: The Conventional Serial Staggered (CSS) scheme.

Farhat and Lesoinne [4] also presented a similar procedure, the *Improved Serial Staggered (ISS)*, which uses the structural velocity and calculates the fluid states at the middle of each time step.

3. Implementation

First of all, some verification tests were made using APDL Verification Manual. Then, an aircraft wing was used to make a mesh convergence test, using four different meshes: 16×10, 32×20, 64×40 and 128×80. These numbers represent the number of panels of the skin in the form *chordwise*×*spanwise*.

The wing has NACA 0010 airfoil and an aspect ratio $\mathcal{AR} = 4$. Two spars are introduced inside the skin at 0.3 and 0.7 chord distance from the leading edge (Figure 3). The material used is steel with $E = 200\ GPa$, $\nu = 0.3$ and $\rho = 7800\ kg/m^3$ and thickness of 10 mm for all surfaces.

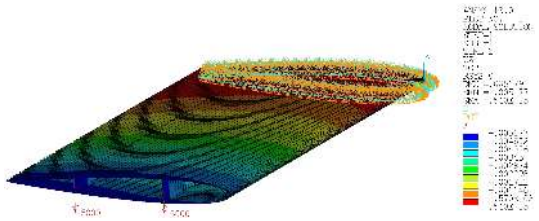

Figure 3: Static test using a wing with two nodal loads of 5000 N (mesh 128×80).

Mesh	Displacement [mm]	Deviation
16×10	-5.387	4.1%
32×20	-5.219	0.8%
64×40	-5.186	0.2%
128×80	-5.177	0.0%

Table 1: Mesh study for the wing steady test.

Table 1 contains a summary of the results. The displacement values are the maximum values for each case. A deviation of the results is calculated in relation to the finer mesh. A mesh having 32×20 panels proves to be a good approximation and still cheap in terms of computational cost.

3.1. Panel Method Validation

In order to get into the panel methods particularities, four programs were created 2DS (two-dimensional steady), 2DU (two-dimensional unsteady), 3DS (three-dimensional steady) and 3DU (three-dimensional unsteady), all coded in MATLAB. The 2DS also uses constant doublets and sources but punctual singularities. It was validated using a *Kármán-Trefftz* airfoil, which has exact solution for potential flow. The 2DU was simply the same program with the time-stepping wake convection.

The 3DS, which is more important for this work, was validated with wind tunnel data and compared with a similar panel method program (called here 3DBalt) both documented in [2].

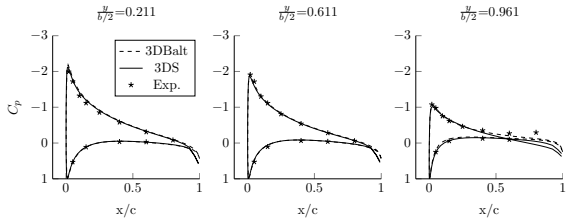

(a) Pressure distributions for the $\alpha = 8.5°$

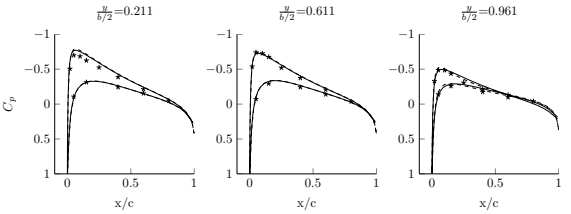

(b) Pressure distributions for the $\alpha = 2.5°$

Figure 4: Comparison of pressure distributions for 3D steady case.

A wing with $\mathcal{AR} = 4$ and NACA 0015 airfoil is here applied. To have a fair comparison, a similar mesh 64×32 panels is used with a cosine distribution on the spanwise direction. In Figure 4, 3DS shows a good approximation of the experimental results, even at the wing tip.

The consequence of the use of a linear Kutta condition can be clearly seen here, since 3DS shows an opened contour at the trailing edge. In contrast, with a converged solution using the iterative pressure Kutta condition, 3DBalt exhibits a fully closed curve.

Moreover, it is presented in Figure 5 a comparison

of the non-dimensionalized circulation (or potential jump) of the wake, which shows good accordance of both panel methods. Herein, the cosine spanwise discretization makes the difference since the circulation changes closer to the wing tip, while it is almost constant close to the wing root. In this case, a wing with $\mathcal{R} = 4$ and NACA 0010 airfoil was simulated.

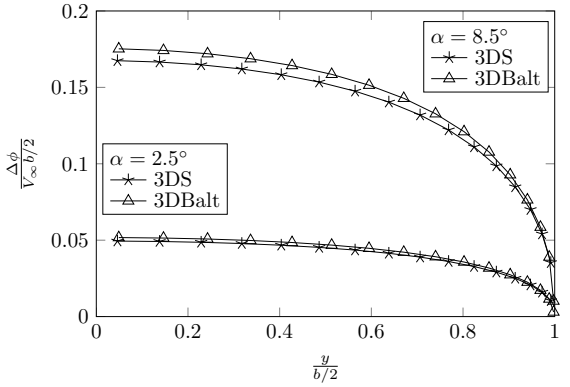

Figure 5: Comparison of the potential jumps along the span of the wing.

For the previous configuration, applying a 6° angle of attack, also the lift and drag coefficients were evaluated for different meshes and they are presented in Table 2.

Mesh	3DBalt		3DS	
	C_L	C_D	C_L	C_D
16×10	0.1082	0.0039	0.08842	0.0038
32×18	0.1024	0.0034	0.09376	0.0064
64×34	0.1002	0.0032	0.09572	0.0074
128×66	0.0993	0.0031	0.09632	0.0079

Table 2: 3D steady results comparison for different meshes.

The results are close between programs. However, while the refinement approximates 3DS to 3DBalt at the lift, it increases the difference in the induced drag predicted by 3DS as well.

3.2. Aeroelastic Design Framework

Next, the both solvers were merged to perform the desired aeroelastic computations. The main script is still coded in MATLAB, which calls APDL and read its results in a very efficient fashion.

Figure 6 presents the main structure of the aeroelastic framework. The input box comprises all the variables defined by user before the computation. Organized in categories, they are:

1. **Fluid** - density, velocity and angle of attack;
2. **Wing** - chord at wing root and tip, x and z coordinates of the point on the leading edge on the wing tip (sweep and dihedral);

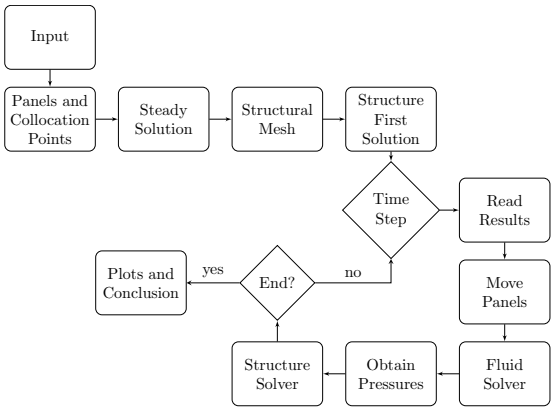

Figure 6: Flowchart illustrating the aeroelastic calculation process.

3. **Mesh** - file with the airfoil coordinates (number of points dictates the number of chordwise panels), number of spanwise panels;
4. **Steady Wake** - initial steady wake angle and length;
5. **Structure** - spars location, material properties, thicknesses, presence of ribs;
6. **Time** - time step size, number of steps;
7. **Method** - Choice of CSS or ISS procedure and the time discretization method for the fluid domain, Backward Euler or Crank-Nicholson.

First of all, the wing panels and collocation points are stored in the respective variables and 3DS program is applied to introduce a steady solution for the specified angle of attack. This will produce the first set of loads.

Next, two lists are created in such a way that APDL is able to read it. One contains the nodes and their position and the second contains the elements and the information needed (nodes, material, section number, element type, and frame of reference). Those lists are saved in files and read in APDL. The difference of the first solution is that at the beginning the wing is at rest. In the subsequent ones, a set of initial conditions (velocity and displacement) is applied using the values of the last substep of the previous structure solution. This assures that one has continuity of the movement.

Figure 7 shows an example of a load case applied on a wing with $\alpha = 4°$, obtained after the preprocessing stage. The elements of the structural mesh were created in such a way that the normals of the skin elements are pointing outwards by the right-hand rule.

After the initialization of the computation, the program enters in a cycle in the time domain. It begins by reading and sorting the results file wrote by

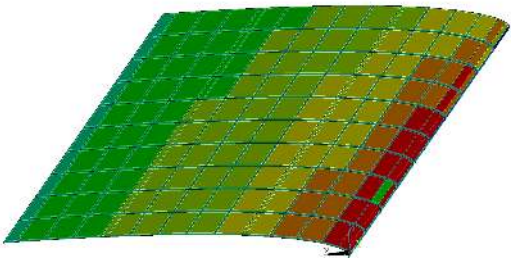

(a) Upper or suction surface

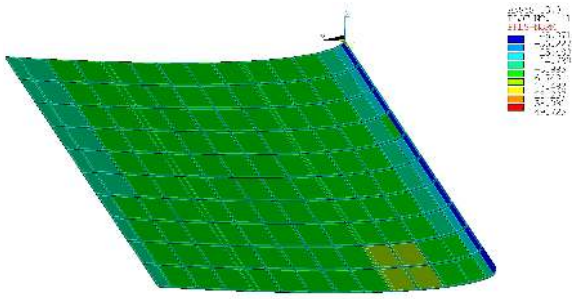

(b) Lower or pressure surface

Figure 7: Example of a load case on an aircraft wing (legend valid for both images).

APDL, that contains the displacements and velocities for all nodes in all the time substeps computed in this visit.

Next, the aerodynamic mesh is updated and introduced together with the previous wake positions and strengths into a fluid solver. The mentioned fluid solver is nothing more than the 3DU program adapted to a function which receives the previous state as input and gives back the velocity field in the next time step.

The pressure field is then computed using Equation (8) and pressure vector are obtained from the dimensionalization of C_p with $\frac{\rho}{2}V_\infty^2$.

This cycle simply continues the solution until the desired time limit is reached. When the last cycle is completed, the last set of results is read. In this moment, some plots can be done to observe the behavior of the wing during the movement.

Figure 8 shows a possible post-processing manner which tracks the evolution of the wake during the whole calculation. This is the (X, Y, Z) frame and the wake is being convected with the flow velocity. The last panel row is wider because it represents the steady initial solution.

4. Results

After having the framework finished, several initial tests were made to reduce the range of input options and have a set of results with physical sense and computationally cheap.

One first study is here presented, which is called

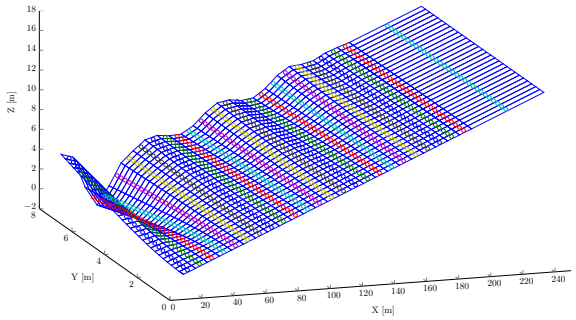

Figure 8: Example of the wake panels after 25 time steps (blue lines are the panel edges and colorful circles are the respective collocation points).

the *Reference Case* (RC). Later several input parameters will be changed and their influence discussed, using the comparison with the RC.

4.1. Reference Case

The same input values used in the APDL static test from Section 3 are here applied, using a 64×30 mesh, $\mathcal{AR} = 15$, NACA 0010 airfoil, two spars at 0.3 and 0.7 chordwise location and the wing being rectangular with $c = 1$ m and no ribs. Moreover, CSS procedure is applied using Backward Euler for the pressure time integration and Newmark in APDL for the structural time discretization.

The fluid density is assumed to be $\rho = 1$ kg/m^3 corresponding to an altitude of 1371 m at standard atmosphere conditions (considering a temperature offset of 20 $°C$), the angle of attack is $\alpha = 4°$ and the fluid velocity $V_\infty = 75$m/s. The initial wake angle is the angle of attack and its length is three time the wing span. The time step is set to 0.1 s.

To be able to track the wing movement, several prints are taken during each structural step in APDL. The vertical displacement and the spanwise rotation of two nodes at the wing tip, one at the leading edge (LE) another at the trailing edge (TE), are plotted in Figure 9(a).

The nodal trajectory of both nodes is almost coincident so the torsion is very low. This is confirmed by Figure 9(b) that shows a maximal rotation of $2 \cdot 10^{-3}$ rad which means roughly 0.1°. Microscopically, the rotational movement has a lot of oscillations. On the other hand it has macroscopically the same period of the vertical displacement. When one is at the minimum displacement, it corresponds to the maximum rotation (positive rotation around Y is using the Right-hand rule, from Z towards X axis, also called nose-up) and vice-versa. So, the torsional movement seams to be damping the bending movement.

However the increase of the wing maximal displacement shows clearly that this velocity is already

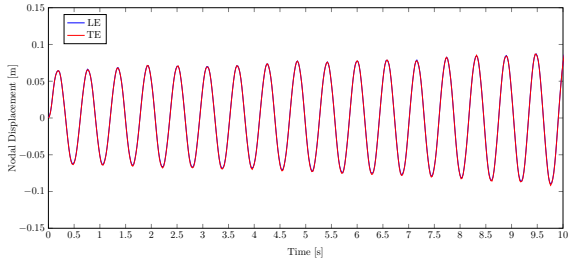

(a) Vertical displacement of LE and TE wing tip nodes.

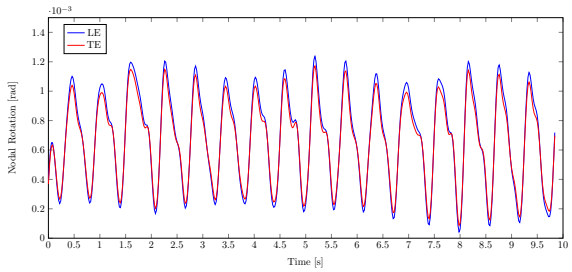

(b) Rotation of LE and TE wing tip nodes.

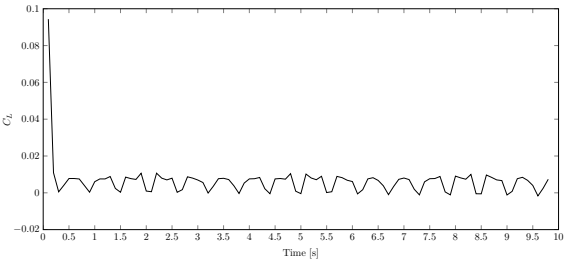

(c) Wing lift coefficient.

Figure 9: Aeroelastic reference results.

higher than the flutter velocity.

Using the peak values, the movement period and frequency are easily obtained. To obtain a consistent value, three values were used at the beginning, middle and end of the movement. The results are summarized in Table 3. Like it was expected, the frequency of the movement is nearly constant during all computation. If one counts the total number of peaks and divides by the respective time, the frequency obtained is 1.7 Hz, so that proves the constancy of the movement.

Time [s]	Frequency [Hz]
0.2 0.76	1.786
8.9 9.48	1.724
16.42 17.02	1.667

Table 3: Period and frequency of the vertical movement of RC.

Figure 9(c) shows the evolution of the lift coefficient with the time. After the initial steady solution, the variation is not very significant, being however possible to see the oscillation caused by the wing movement, which varies with approximately the same frequency than the nodal displacement from Figure 9(a). Furthermore, lift positive peaks correspond to rotation positive peaks, which is physically correct.

4.2. Free Stream Velocity

The first parameter to study is the free stream velocity. Figures 10(a) and 10(b) show the LE node behavior. The TE was suppressed because its movement is almost coincident with the LE.

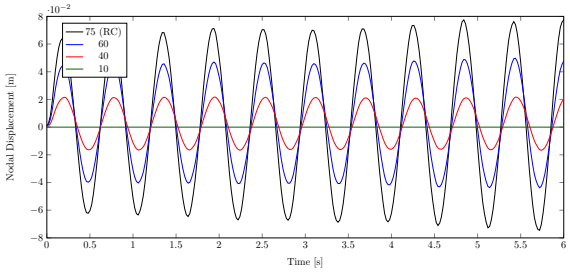

(a) Vertical displacement of LE wing tip node.

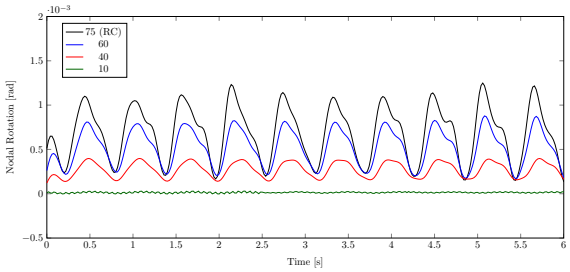

(b) Rotation of LE wing tip node.

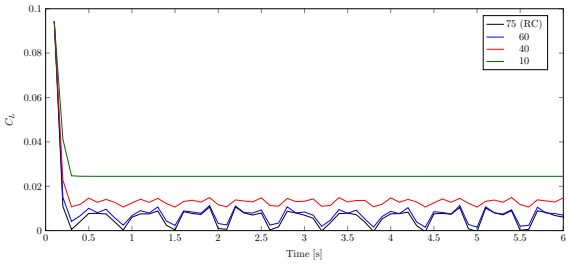

(c) Wing lift coefficient.

Figure 10: Influence of the free stream velocity [m/s] in the aeroelastic wing behavior.

The graph for the 60 m/s is still smoothly divergent, while the 40 m/s has practically zero damping. So it is concluded that the flutter velocity is around 40 m/s. With the 10 m/s, the wing still oscillates but with displacements of the order 10^{-4} m, so it cannot be seen here.

In Figures 10(a) and 10(b), it is possible to see the

bending-torsion coupling, since both movements have the same frequency, however opposite polarity (i.e. 180 degrees phase difference). Watching also 10(c), one can confirm that the positive rotation is a nose-up position, since the lift coefficient has also a maximum. Moreover, the lift has the same frequency of the rotational and bending movements.

As it is expected, the frequency of the movement does not change with the free stream velocity. As it will be seen later, other parameters will have this effect.

4.3. Spar Location

The next test is made changing the location of the two wing spars. As it will be seen, by moving the spars in the chordwise direction towards one of the edges, one is changing the wing torsional stiffness, maintaining the bending movement frequency very similar.

Three computations were done with the spars at 0.7 and 0.9 chords, which means close to the trailing edge; 0.1 and 0.3, close to the LE; 0.45 and 0.55, closer to each other than the RC (0.3 and 0.7 chords).

In the first case, the wing movement is largely divergent and the vertical displacement reaches the order of meters in a few seconds, so it will not be plotted here. This result was expected since, in practice, what was done was to move away the twist center from the aerodynamic center. This causes torsional divergence [8] and, consequently, also bending divergence.

Figure 11 shows the results for the other cases compared with the RC. 11(a) confirms that the bending frequency was not affected. However, by placing the spars closer to each other at the wing center, the flutter velocity increased and the nodal maximum vertical displacement is decreasing very slow in this case.

The lift coefficient is also not significantly affected, maintaining also the frequency accordingly to the displacement.

The big difference is the torsional movement when the spars are pushed towards the LE, which places the center of twist ahead of the aerodynamic center. As it can be seen in Figures 11(a) and 11(b), the bending movement is still similar but a torsional divergence with higher frequency appears.

4.4. Skin Density

After making changes in the flow, in the wing spar and in the sweep angle, the next two parameters to change are related to material constants. Like it was stated before, the material changes in the spars did not affect significantly the wing dynamic behavior, so only the changes in the skin are presented here.

Herein, the influence of the density is investigated. Taking a look back at Chapter **??**, the

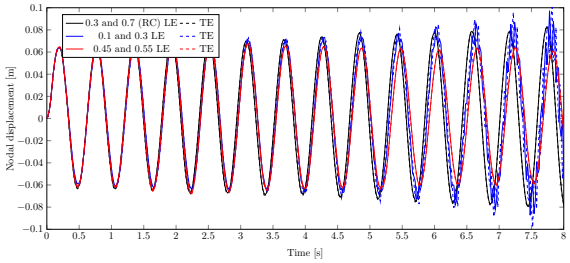

(a) Vertical displacement of LE wing tip node.

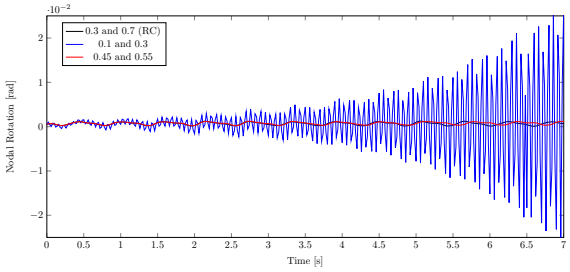

(b) Rotation of LE wing tip node.

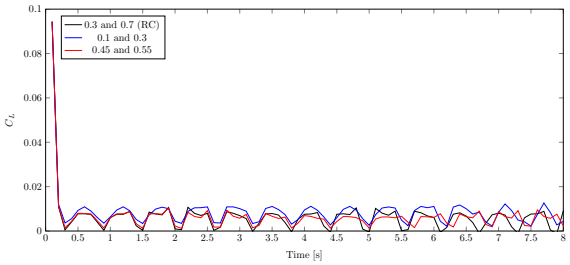

(c) Wing lift coefficient.

Figure 11: Influence of the spars location (measured in chords) in the aeroelastic wing behavior.

density will have influence on the structural mass matrix M defined in Equation (**??**). Equation (1) shows that M influences the inertial forces, since it is multiplied by the acceleration vector $\ddot{\vec{u}}$. So, the higher the density, the higher the inertial forces.

In Figure 12(a), one can immediately see that the density influences mainly the frequency of the vertical movement. Table 4 summarizes the frequency calculation for the three computations.

Density [kg/m^3]	Frequency [Hz]
5000	2.10
7800	1.72
10000	1.54

Table 4: Frequency of the vertical movement for changing material density.

Figure 12(a) also shows that reducing density also helps the wing to diverge, since the peak values increase in comparison with the RC. In reverse, the heavier wing has more inertia causing the amplitude

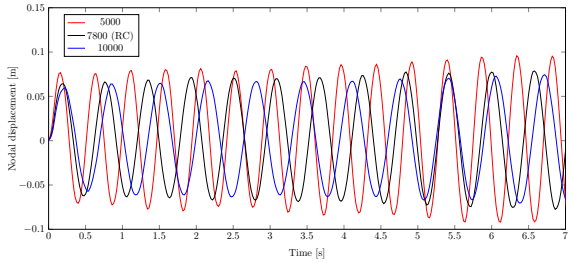

(a) Vertical displacement of LE wing tip node.

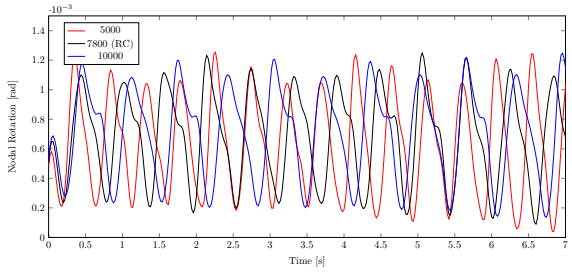

(b) Rotation of LE wing tip node.

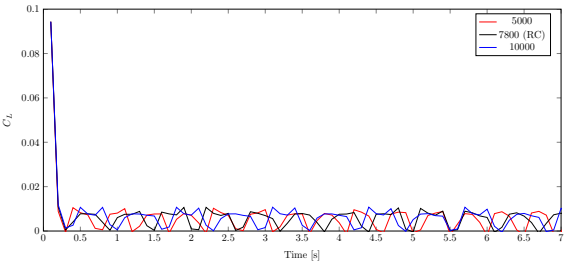

(c) Wing lift coefficient.

Figure 12: Influence of the skin density [kg/m^3] in the aeroelastic wing behavior.

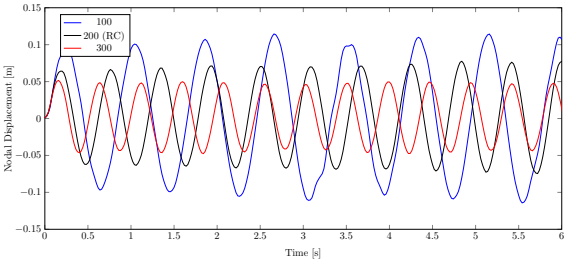

(a) Vertical displacement of LE wing tip node.

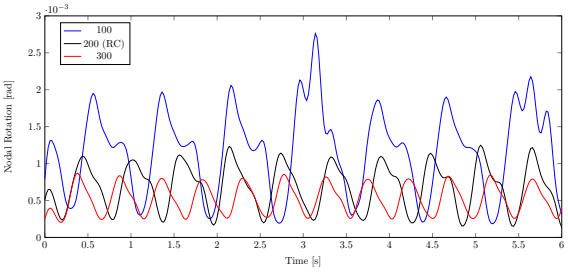

(b) Rotation of LE wing tip node.

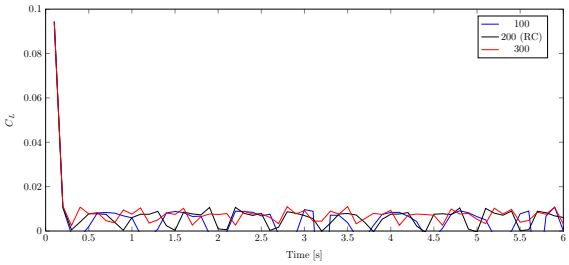

(c) Wing lift coefficient.

Figure 13: Influence of the skin Young modulus [GPa] in the aeroelastic wing behavior.

of the oscillations to be smaller.

Figures 12(b) and 12(c) basically show accordance to 12(a) in terms of the frequency, like it was expected.

4.5. Skin Young Modulus

Next, the influence of the elasticity or Young modulus E will be tested. Increasing E makes the material more stiff, while decreasing makes it more elastic.

Having the reference value of 200 GPa, two more computations were made with 100 and 300 GPa.

The results are clear in Figure 13. As soon as one decreases the Young modulus, both bending and torsion amplitudes will increase, likewise the period. In this specific case, the increase to 300 GPa also transforms the movement to convergent, since the amplitude is decreasing with the time.

The lift coefficient does not suffer a significant change, besides the frequency which is in accordance with Figures 13(a) and 13(b).

5. Conclusions

An aeroelastic design framework was presented for the study of aircraft wings. It is composed by three main parts: the structure solver APDL, the fluid solver a panel method coded in MATLAB and a coupling procedure also in MATLAB which controls the other two parts.

The fluid solver was fully developed in MATLAB, going from the steady two-dimensional to the unsteady three dimensional problem, being the two-dimensional case validated with exact results from the potential theory and the three-dimensional validated with wind tunnel tests. Furthermore, the results were also compared with another panel method program presented in [2] and with XFOIL.

The mesh nodes and elements, the material constants, the section types and thickness, the loads and the initial conditions are saved to files by MATLAB and then read from APDL, which, in turn, writes the nodal displacements, velocities and rotations to another files. This method proved to be very efficient and reliable.

The FSI normally generates some issues like the transfer of loads and displacements, the frame of reference and the added mass. The first two were very simplified, since the fluid solver used made it possible to use the same grid in both domains, having only left the Load Lumping issue, which was proved to be accurate. The latter just influences cases when the fluid and structure densities are comparable, for instance blood flows inside veins.

The aeroelastic framework created starts with a fluid steady solution for the values input by the user. Then, it generates the structural mesh which remains the same during all the computation. After the first structural solution, a time cycle starts performing a defined number of cycles with the same time step for both fluid and structure solver. The latter has however the possibility to have substeps to track the body movement more precisely.

In dynamic aeroelasticity, it is usual to calculate the flutter velocity. Therefore that was the first parameter to vary and the results show that it is possible to calculate an approximate flutter velocity for an aircraft wing. The other tests showed that the spar position changes the wing center of twist, the sweep angle changes the coupling between the bending and torsion movements, the skin density influences the inertial forces and consequently the period and amplitude of the bending movements, as well as the Young modulus which influences the material stiffness or elasticity.

As it was said before, the absence of structural elements like stringers, forced the use of very thick skin elements. A more realistic step would be to add elements to the structural mesh to simulate the stringers.

APDL Batch run proved to be efficient but it also caused some problems having errors arising from some conflicts with Windows. A certainly great improvement would be to program a structural transient solver in MATLAB which would be easier to couple with the panel method.

Two coupling procedures were tested and also two fluid time integration schemes. The possibility of having both solvers coded in MATLAB would make possible a monolithic approach with different discretization methods.

A very important step would be to construct a wing model and obtain wind testing data in order to validate the results computed by this framework.

Further work can also be pursued in shape or topology optimization using the aeroelastic analysis framework here developed and presented. Tackling problems of flutter speed maximization of an aircraft wing with constraints in weight is something of utmost importance in very high performance aircrafts.

Acknowledgements

I want to express my gratitude for my supervisor Professor André Marta for his total dedication since our first talk to the final presentation of this thesis. His large knowledge was definitely the key to guide me through this task. Also to Professor Luís Eça for his pertinent and helpful advices and Doctor João Baltazar for kindly providing his PhD thesis and his results which were determinant to the validation of my aerodynamic calculations.

References

[1] ANSYS, Inc. (2010, November). *Theory Reference for the Mechanical APDL and Mechanical Applications*. Canonsburg, PA: ANSYS, Inc. Release 13.0.

[2] Baltazar, J. M. R. D. C. (2008, September). *On the modelling of the potential flow about wings and marine propellers using a boundary element method*. PhD dissertation, Instituto Superior Técnico (IST).

[3] Bisplinghoff, R. L., H. Ashley, and R. L. Halfman (1996). *Aeroelasticity* (First ed.). Dover Books on Physics. Mineola, New York: Dover Publications, Inc.

[4] Farhat, C. and M. Lesoinne (2000). Two efficient staggered algorithms for the serial and parallel solution of three–dimensional nonlinear transient aeroelastic problems. *Computer Methods in Applied Mechanics and Engineering 182*(3 - 4), 499 – 515. doi:10.1016/S0045-7825(99)00206-6.

[5] Hirsch, C. (2007). *Numerical Computation of Internal and External Flows* (Second ed.), Volume 1 Fundamentals of Computational Fluid Dynamics. Oxford: Butterworth-Heinemann.

[6] Hirschel, E. H., H. Prem, and G. Madelung (2004). *Aeronautical Research in Germany From Lilienthal until Today* (First ed.). Berlin Heidelberg: Springer-Verlag.

[7] Katz, J. and A. Plotkin (2001). *Low-Speed Aerodynamics* (Second ed.). Number 13 in Cambridge Aerospace Series. Cambridge University Press.

[8] Megson, T. H. G. (2007). *Aircraft Structures for Engineering Students* (Fourth ed.). Elsevier Aerospace Engineering Series. Oxford: Butterworth-Heinemann.